

Increasing ultrasound field-of-view with reduced element count arrays containing large elements

Mick Gardner,^a Rita J. Miller, and Michael L. Oelze

Electrical and Computer Engineering, University of Illinois Urbana-Champaign, Urbana, IL 61801, USA

Several applications of medical ultrasound can benefit from a larger imaging field of view (FOV). This study is aimed at increasing the FOV of linear array probes by increasing the element size rather than the element count. To investigate larger FOV, this study used coupled elements to imitate a larger element size. The effects of coupling on array beam patterns are examined with Fourier transforms of elements. The effects of coupling on resolution, contrast, and speckle signal-to-noise ratio are examined through phantom images and in-vivo images of a rabbit tumor reconstructed with plane-wave compounding. Furthermore, a positioning system was used to acquire data from a virtual large aperture with 120 mm FOV and 128 elements, collected in sections with a single probe. This study also investigates the Null Subtraction Imaging (NSI), Sign Coherence Factor (SCF), and Minimum Variance (MV) beamformers for regaining resolution lost by an increased F-number with large elements. The MV beamformer, while the most computationally expensive, was best for improving resolution without increasing speckle variance, decreasing Full-Width at Half-Max (FWHM) estimates of wire targets from 0.78 mm with DAS on a 2.5 wavelength element size to 0.54 mm with MV on a 5 wavelength element size.

[<https://doi.org/DOI number>]

[XYZ]

Pages: 1–12

I. INTRODUCTION

Increasing the field of view (FOV) of ultrasound is of major interest in the medical ultrasound community for applications such as abdominal (Kim *et al.*, 2003), muscle (Noorkoiv *et al.*, 2010), spine (Huang *et al.*, 2019), and vascular imaging (Kang *et al.*, 2020; Wang *et al.*, 2022). Many structures and organs in the human body are too large to fit in a single image with current ultrasound probes. This is especially true for the case of 3D ultrasound imaging using a 2D matrix array, where the field-of-view is often severely limited by a small probe footprint with an extremely high channel count. Therefore, there is a need for an increased field-of-view to capture a full region of interest. Several approaches exist to increasing the FOV.

One such approach is to add more elements to the array (Bottenuis *et al.*, 2020; Foiret *et al.*, 2022). Adding more elements will increase the FOV by increasing the probe footprint, and can also provide benefits to resolution from an increased F-number. However, cost, data processing, and electrical connections to the back-end system all become a burden for very high channel count arrays. Two approaches exist for handling high channel counts: multiplexing and micro-beamforming. With multiplexing, the system switches between subsections of the array for different transmit/receive events, so a high channel count probe can be connected to a

lower input count system (Yu *et al.*, 2020). The primary trade-off with multiplexing is the frame rate. For a probe with a 4 x 1 multiplexer, anywhere between 4 - 16 transmission events are needed for a single acquisition (e.g. plane-wave angle) (Chavignon *et al.*, 2022). With micro-beamforming, elements are grouped into patches, beamforming within the patches is done on ASICs inside the transducer handle, then beamforming across patches is done by the back-end system (Savord and Solomon, 2003). This way the probe only needs one connection per patch back to the system. However, micro-beamformers are suboptimal for ultrafast imaging, due to quantization and approximation of the time delay calculations in the ASICs (Castrignano *et al.*, 2025).

Alternative approaches seek to increase the FOV without an increased element count. For example, convex and phased arrays use limited elements, but have FOVs that extend far beyond their footprint due to the convexity or beam steering. A challenge with these probes is maintaining resolution over the FOV with scan lines that spread out with depth (Kang *et al.*, 2020). Panoramic images, sometimes called extended FOV (EFOV) ultrasound, presents another option for increasing the FOV (Kim *et al.*, 2003; Poon and Rohling, 2006). In this method, the probe is translated to multiple locations and images from the separate acquisitions are registered to create a larger combined image. However, this method could only create static images with the increased FOV, not real-time video data, because it requires acquisitions from multiple locations. Array sparsity, in other words breaking array periodicity, has also been investigated as a

^amickhg2@illinois.edu

method for reducing the element count on both 1D and 2D arrays (Gavrilov *et al.*, 1997; Ramalli *et al.*, 2022). This is usually achieved by deactivating select elements from fully populated arrays. One issue with sparsity is decreased transmit power (lower SNR) due to low element count and small elements. Also, the break in periodicity creates higher side lobes, reducing contrast.

Another approach to increasing the field of view without increased element count is the use of larger elements. Recently, for the case of 3D imaging, row-column arrays were introduced which consist of 2 orthogonal arrays of very large line elements accessed by row or column index (Jensen *et al.*, 2022). This has allowed for construction of much larger 2D arrays with wider FOV and reduced element count. Another group has tested large 2D apertures for ultrasound localization microscopy (ULM) that use large, circular elements (Favre *et al.*, 2022, 2023). In this approach, to address issues with resolution from an increased F-number of highly directive elements, diverging acoustic lenses were placed over individual elements to widen the directivity and regain resolution (Favre *et al.*, 2022). However, lenses did not eliminate grating lobes.

Rather than using lenses, a simpler solution could be to use adaptive or non-linear beamformers suitable for the task of regaining resolution lost by a narrowed directivity. The Null Subtraction Imaging (NSI) beamformer is an emerging non-linear beamforming technique that can greatly improve resolution by imaging with beam nulls instead of a main lobe (Agarwal *et al.*, 2019; Kou *et al.*, 2023). NSI has also been used to mitigate grating lobes in rat tumor images (Kou *et al.*, 2022) and on large pitch arrays (Gardner *et al.*, 2024). The minimum variance (MV) beamformer has been shown to greatly improve resolution in ultrasound B-mode images (Synnevag *et al.*, 2007). Lastly, the Sign Coherence Factor (SCF) beamformer was introduced as a computationally inexpensive version of Phase Coherence Factor (PCF) which was made to reduce grating lobes and can also improve resolution (Camacho *et al.*, 2009a,b).

This study is aimed at increasing the FOV of ultrasound by increasing the element size, then using an appropriate beamformer for regaining resolution and mitigating grating lobe artifacts. We see greatest potential application to the case of 2D imaging with large, square elements. To test our approach, we examined larger elements on a 1D probe, using coupled elements to imitate a larger element width. The element coupling involved transmitting blocks of adjacent elements at the same time, then summing their receive radio-frequency (RF) channel data so that they acted as if they were one element. We have examined array beam patterns resulting from coupled elements. We also performed phantom experiments to see the effects of coupled elements on image quality, as well as compared conventional delay-and-sum (DAS) beamforming with NSI, SCF, and MV beamformers for restoring resolution. To show how this approach can lead to larger apertures and FOVs, we also collected data from a virtual large aperture, with data collected in

sections using a standard probe on a positioning system. Plane-wave transmissions were used for all experiments because they can provide much higher frame rates than traditional line-by-line scanning.

II. BACKGROUND THEORY

Here we present a brief analysis on the effects of large elements on the beam pattern of a linear array. The beam pattern is the product of the directivity (sometimes called an element factor) and an array factor, as in

$$B(\theta) = H(\theta)G(\theta) \quad (1)$$

where θ is the angle of arrival of a signal, $H(\theta)$ is the array factor, $G(\theta)$ is the element factor, and $B(\theta)$ is the final beam pattern.

The array factor for an unsteered point-source array at a single frequency is given by the following equation

$$H(\theta) = \frac{1}{N} \frac{\sin\left(\frac{N}{2}kds\sin(\theta)\right)}{\sin\left(\frac{1}{2}kds\sin(\theta)\right)} \quad (2)$$

where θ is the direction of arrival, N is the number of elements in the array, k is the wave-number, and d is the array pitch (spacing between elements). Note that this equation is the Fourier transform of a discrete rectangle function representing element locations. When d is greater than a wavelength, grating lobes will appear in the unsteered array factor, with locations found by setting the denominator of Eq. 2 equal to zero and solving for θ :

$$\theta = \pm \sin^{-1} \left(\frac{m\lambda}{d} \right) \quad (3)$$

where λ is the wavelength, and m is an index. This equation is valid for values of m where $m\lambda/d$ is less than 1.

The element directivity for a single frequency is given by the formula

$$G(\theta) = \text{sinc} \left(\frac{Wks\sin(\theta)}{2} \right) = \frac{\sin(Wks\sin(\theta)/2)}{Wks\sin(\theta)/2} \quad (4)$$

where W is the width of an element. Note that this equation is the Fourier transform of a continuous rectangle function representing a rectangular element. When the width W is greater than a wavelength, nulls will appear in the directivity, with locations found by setting the numerator of Eq. 4 equal to zero and solving for θ :

$$\theta = \pm \sin^{-1} \left(\frac{m\lambda}{W} \right). \quad (5)$$

With the multiplication in Eq. 1, it is desirable to line up element factor nulls with array factor grating lobes so that grating lobes are canceled. From Eqs. 3 and 5, that leads to $W = d$. This would represent a kerf of zero, where $\text{kerf} = d - W$, representing the empty space between adjacent element edges. Of course, this case does not represent an array, but one single line element. For a linear ultrasound probe, the kerf is the width

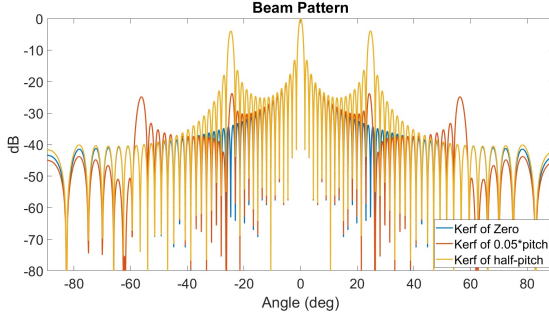


FIG. 1. Beam patterns for 16-element arrays with a pitch of 2.5 wavelengths and different kerfs. A kerf of 0 cancels all grating lobes, but it is not an array (blue). A kerf that is half the pitch cancels the second grating lobe but leaves very high first grating lobes (yellow). The minimum kerf that can be manufactured is optimal to minimize all grating lobes (orange).

of the saw used to cut the piezoelectric material into separate elements. The kerf will slightly push out the nulls in the element factor, reintroducing grating lobes as displayed in Figure 1. The minimum kerf that can be manufactured is optimal for minimizing grating lobes, but low grating lobe artifacts will still exist. As the pitch of the array is increased, more grating lobes will appear (Eq. 3).

Also, larger elements make the element factor more narrow (Eq. 4), which raises the achievable F-number of the array (Perrot *et al.*, 2021). A higher F-number widens the main lobe, as displayed in Figure 2. Therefore, a loss in image resolution is expected with larger elements. These issues with resolution and grating lobes motivate the use of adaptive and non-linear beamformers which can improve resolution and reduce grating lobes (Camacho *et al.*, 2009a; Gardner *et al.*, 2024; Kou *et al.*, 2022; Synnevag *et al.*, 2007).

Lastly, this paper made use of coupled elements to imitate larger elements. The coupled elements still had kerf gaps in between, which a large element of the same width would not have. The Fourier transforms of the elements shows the effect these gaps will have on the directivity, displayed in Figure 3. In the Fourier transforms, only small differences in the side lobes are observed, while the main lobes are basically identical. Therefore, coupled elements make a good approximation of a single, large element with the same width.

III. METHODS

A. Experiment setup

1. Element Coupling

For all experiments, an Ultrasonix L14-5/60 probe (Ultrasonix, BC, Canada) was used, connected to a Verasonics Vantage 128 system (Verasonics, Inc., Kirkland, WA, USA). Element coupling was performed on both

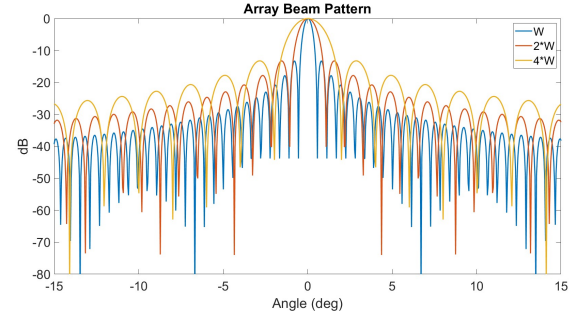


FIG. 2. Array beam patterns for different element widths. The larger element size/narrower directivity raises the array F-number, resulting in a wider main lobe for the array beam pattern.

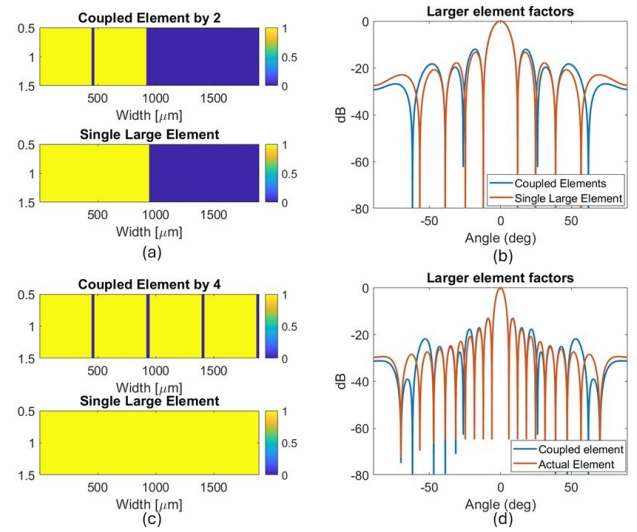


FIG. 3. Directivities of coupled elements (with kerf gaps) compared to directivities of corresponding large elements. (a) Coupled element by 2 (top) and large element (bottom) with corresponding directivities in (b). (c) Coupled element by 4 (top) and large element (bottom) with corresponding directivities in (d). The directivities of the coupled elements match closely to those of the large elements, meaning coupled elements are a good approximation of a large element.

transmit and receive so that blocks of adjacent elements would act as if they were one large element. Elements were coupled by averaging their transmit delays and summing their received channel data. For a steered plane-wave, the transmit profiles of coupled and uncoupled elements looked something like Figure 4, where blocks of adjacent elements fired at the same time. Then, the receive RF traces within each block were summed together without applying any time delays to create the coupled RF trace. Coupling factors of 1, 2, and 4 were tested to divide evenly the 128-element array. These coupling factors resulted in effective element sizes of 2.5 wavelengths,

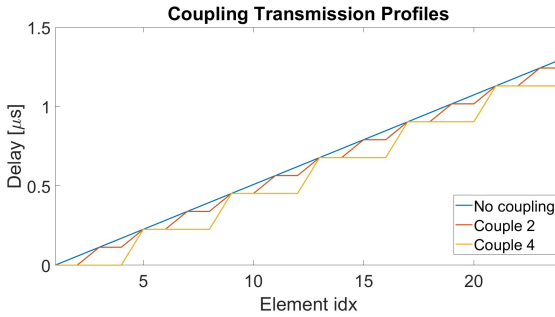


FIG. 4. Example transmission profiles of uncoupled (blue), coupled by 2 (orange), and coupled by 4 (yellow) arrays for a positive plane-wave steering angle. Blocks of consecutive elements fire at the same time for coupling by 2 and 4, making the jagged steps in the transmit delay profile.

5 wavelengths, and 10 wavelengths respectively when operating the probe at its standard center frequency of 7.81 MHz.

To see the effects of larger elements on resolution and contrast, we scanned a CIRS Model 539 ATS General purpose phantom (Computerized Imaging Reference Systems, Norfolk, VA, USA). Data was acquired of wire targets and anechoic regions. Additionally, we scanned the abdomen of a New Zealand White Rabbit to examine the effects of coupling *in vivo*. Animal procedures were approved by the Institutional Animal Care and Use Committee at the University of Illinois at Urbana-Champaign. Rabbits were anesthetized using isoflurane, then the fur on the rabbit's abdomen was shaved for imaging.

2. Increased aperture size

This experiment was performed to demonstrate how larger elements can lead to larger apertures with reduced element counts. The L14-5/60 probe and the ATS phantom were placed on a Daedal positioning system (Parker Hannifin Corp., Cleveland, Ohio, USA), where the probe was fixed in place, while the phantom was on a sliding table allowing it to move laterally underneath the probe (see Figure 5). A few centimeters of degassed water were placed in the top of the ATS phantom to ensure good acoustic transmission into the phantom. The basic idea was to move the phantom to two positions under the probe, so the probe could transmit and collect data as if it were sections of an aperture of twice the size. The L14-5/60 probe is made up of $N = 128$ elements with a pitch $p = 472 \mu\text{m}$. Therefore, the distance the probe had to move (or equivalently, the phantom underneath it) to be aligned as a different section was $Np = 60.416 \text{ mm}$. Transmit delay profiles were designed for a virtual aperture of 120 mm with 128 elements. Then, corresponding halves of the transmission profile were fired from the L14-5/60 with elements coupled by 2 for either position (see Figure 6). Received channel data was then concatenated to be beamformed as if it came from a single aperture.

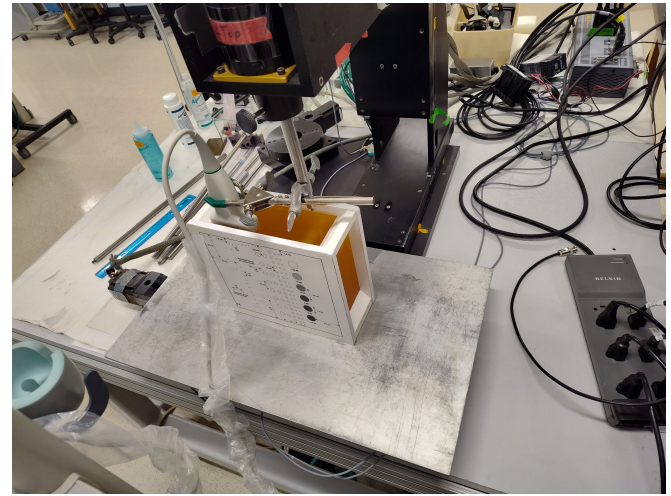


FIG. 5. Photograph of the imaging setup for acquiring data from a virtual large aperture. The probe was held in place while the phantom was moved on the sliding table beneath it.

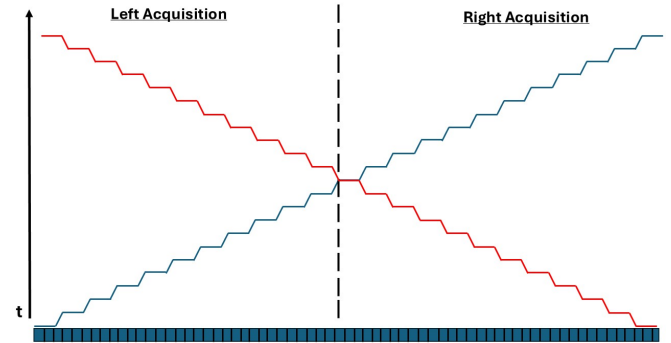


FIG. 6. A diagram of possible transmission profiles for either half of the virtual large-aperture acquisition with coupled elements. Blue represents a plane-wave steered in the positive θ direction, while red is the negative θ direction.

B. Beamforming

1. Delay and sum

Delay-and-sum (DAS) beamforming is the conventional beamforming method used on all ultrasound scanners. For this study, DAS was implemented on a pixel grid with spacing of $200 \mu\text{m}$ in axial and lateral directions. Acquired radio-frequency (RF) signals were demodulated into In-phase/Quadrature (IQ) data before beamforming. For each pixel (x, z) , the round trip time of flight is given by

$$\tau(x, z) = \frac{D_{TX}(x, z) + D_{RX}(x, z)}{c} \quad (6)$$

where $\tau(x, z)$ is the round trip time, $D_{TX}(x, z)$ and $D_{RX}(x, z)$ are the transmit and receive distances respectively, and c is the sound speed. For a steered plane wave,

Array	θ_{max} (deg)	Step size (deg)	n_t	F
L14-5/60 Couple 1	11	0.187	118	2.6
L14-5/60 Couple 2	5.3	0.187	58	5.2
L14-5/60 Couple 4	2.6	0.187	28	10.7
Virtual Large Aperture	5.4	0.0935	116	5.2

TABLE I. Table of angle sets for each coupling factor on the L14-5/60 as well as the virtual large aperture. The second column, θ_{max} , is the maximum steering angle. The fourth column, n_t , is the number of plane-wave angles. The fifth column, F , is the array F-number.

the transmit distance is given by (Montaldo *et al.*, 2009)

$$D_{TX}(x, z) = x \sin(\theta) + z \cos(\theta) \quad (7)$$

where θ is the steering angle. The receive distance is

$$D_{RX}(x, z) = \sqrt{(x_n - x)^2 + z^2} \quad (8)$$

where x_n is the lateral location of element n . Once proper time delays are applied, elements are summed coherently, as in

$$y(x, z) = \sum_{n=1}^N A(n) IQ_n(\tau(x, z)) e^{-2\pi j f_0 \tau(x, z)} \quad (9)$$

where $y(x, z)$ is the beamformed output, $A(n)$ is an apodization function such as rectangular or Hamming, IQ_n is the received IQ data from channel n , and f_0 is the center frequency of the transmitted pulse. The array F-number was estimated from the -3 dB point of the element directivity (Perrot *et al.*, 2021)

$$F = \frac{1}{2 \tan(\alpha)} \quad (10)$$

where α is the the -3 dB point.

Plane-wave angle sets were chosen for each coupling factor using the method proposed by (Montaldo *et al.*, 2009). In this method, the plane-wave angle set is given by

$$\theta_i = \arcsin(i\lambda/L) \approx i\lambda/L \quad (11)$$

for $i = -(n_t - 1)/2, \dots, (n_t - 1)/2$, where λ is the wavelength, L is the total aperture size, and n_t is the number of transmissions. The number of transmissions needed is given by

$$n_t = \frac{L}{\lambda F}. \quad (12)$$

Resulting angle sets for each coupling factor on the L14-5/60 as well as the virtual large aperture are detailed in Table I.

2. Null Subtraction imaging

Null Subtraction Imaging (NSI) involves apodizing the DAS beamformed data with three different apodizations, then incoherently summing the outputs (Agarwal

et al., 2019). The first is a zero-mean (ZM) apodization, given by

$$A_{ZM}(n) = \begin{cases} 1, & 1 \leq n < \frac{N}{2} \\ -1, & \frac{N}{2} \leq n \leq N \end{cases} \quad (13)$$

where N is the number of elements in the receive aperture. Two direct-current (DC) apodizations are given by applying an offset to the ZM apodization

$$A_{DC1}(n) = A_{ZM}(n) + dc \quad (14)$$

$$A_{DC2}(n) = A_{ZM}(n) - dc \quad (15)$$

where dc is a constant, set to 0.5 for all experiments. An offset of 0.5 was chosen empirically to balance resolution increase with speckle variance increase (Agarwal *et al.*, 2019). Beamformer outputs resulting from the three apodizations are then envelope detected and applied in the following equation

$$E_{NSI} = \left| \frac{E_{DC1} + E_{DC2}}{2} - E_{ZM} \right| \quad (16)$$

where E_{NSI} is the final NSI envelope, E_{DC1} and E_{DC2} are the DC offset envelopes, and E_{ZM} is the zero-mean envelope. Plane-wave compounding was done coherently on the three apodizations separately before envelope detection (Agarwal *et al.*, 2019).

3. Sign Coherence Factor

The Sign Coherence Factor (SCF) is a quantized version of the Phase Coherence Factor (PCF) where the standard deviation of the phase is estimated only from the sign bit on the aperture data (Camacho *et al.*, 2009b). In this case, the standard deviation of the phase is calculated for a pixel (x, z) by

$$\sigma(x, z) = \sqrt{1 - \left(\frac{1}{N} \sum_{n=1}^N b_n(x, z) \right)^2} \quad (17)$$

where N is the number of elements in the receive aperture, and b_n is the sign of the data from element n . For IQ data, the “sign” is given by

$$b_n(x, z) = \begin{cases} 1, & |\phi| \leq \frac{\pi}{2} \\ -1, & |\phi| > \frac{\pi}{2} \end{cases} \quad (18)$$

where ϕ is the phase angle of the IQ data. The SCF is then calculated as

$$SCF(x, z) = |1 - \sigma(x, z)|^p \quad (19)$$

where p is a parameter for tuning the sensitivity. The parameter p was set to 1 for all experiments. The value $SCF(x, z)$ is then multiplied by the value of the DAS beamformed envelope at location (x, z) . To ensure more accurate estimate of the coherence factor, spatial compounding was performed on the channel data first before estimation of the SCF.

4. Minimum Variance

The Minimum Variance (MV) beamformer adaptively chooses optimal apodization weights for minimizing variance (power) in beamformer output while maintaining unit gain at the focal point (Synnevag *et al.*, 2007). Those weights are given by

$$\mathbf{w} = \frac{\hat{R}(x, z)^{-1} \mathbf{a}}{\mathbf{a}^H \hat{R}(x, z)^{-1} \mathbf{a}} \quad (20)$$

where \mathbf{w} is the desired apodization, $\hat{R}(x, z)$ is the estimated spatial covariance matrix of the time-delayed channel data for pixel (x, z) , and \mathbf{a} is a vector where all values are 1. The spatial covariance matrix was estimated using spatial smoothing, as in

$$R(x, z) = \frac{1}{N - M + 1} \sum_{l=0}^{N-M} X_l(x, z) X_l^H(x, z) \quad (21)$$

where

$$X_l(x, z) = [x_l(x, z), \dots, x_{l+M-1}(x, z)]^T \quad (22)$$

is the vector of channel data in a sub-array, N is the number of receive elements, and M is the sub-array length set to $N/2$. Furthermore, diagonal loading was performed on the spatial covariance matrix as in

$$\hat{R}(x, z) = R(x, z) + \epsilon I \quad (23)$$

where I is the identity matrix, and ϵ is the diagonal loading factor. The ϵ factor was set to $\epsilon = \Delta \cdot \text{tr}\{R(x, z)\}$, where Δ is a constant and $\text{tr}\{\cdot\}$ is the trace. Then, Δ was set to $\frac{1}{10M}$. Spatial compounding was performed before beamforming, so that $\hat{R}(x, z)$ was only estimated and inverted once from compound channel data to minimize the computation time and ensure a more accurate estimate. Finally, the beamformed output was computed as

$$y(x, z) = \frac{1}{N - M + 1} \sum_{l=0}^{N-M} \mathbf{w}^H X_m(x, z). \quad (24)$$

C. Quality metrics

Image quality was evaluated using several metrics. The most important for our study is resolution, estimated as the Full-Width at Half-Maximum (FWHM) of wire targets. This was estimated from the width between the -6 dB points in lateral profiles of wire targets.

Other important quality metrics estimate the contrast of images. The most simple metric of contrast is the contrast ratio (CR), often simply referred to as “contrast.” This is simply the dB difference of means between some region of interest (ROI), such as an anechoic target, and a nearby region of the speckle background. This metric essentially represents the visual contrast of an image, describing what a human might observe. It is measured as

$$C = 20 \log_{10} \left(\frac{\mu_i}{\mu_o} \right) \quad (25)$$

where C is the contrast, and μ_i and μ_o are the mean envelope values inside and outside a ROI respectively. A more objective metric for contrast is the generalized contrast-to-noise ratio (gCNR), defined from the overlapping area of the histograms of two regions (Rodriguez-Molares *et al.*, 2020). The gCNR is defined as

$$gCNR = 1 - \int_{-\infty}^{\infty} \min_x \{p_i(x), p_o(x)\} dx \quad (26)$$

where $p_i(x)$ and $p_o(x)$ are the histograms of the envelopes in some ROI and the background respectively. The gCNR is resilient against dynamic range changes and speckle variance, and thus gives a more objective metric for evaluating contrast improvement between different beamforming algorithms (Rodriguez-Molares *et al.*, 2020).

Finally, speckle statistics were evaluated using the speckle signal-to-noise ratio (sSNR). This ratio is defined as

$$sSNR = |\bar{A}| / \sqrt{var(A)} \quad (27)$$

where \bar{A} is the mean of some speckle region, and $var(A)$ is the variance in that region. Fully developed speckle will have an sSNR value of 1.91 (Wagner *et al.*, 1983). The lower the sSNR value, the less developed the speckle. The NSI, SCF, and MV beamformers are all known to increase speckle variance (Agarwal *et al.*, 2019; Camacho *et al.*, 2009b; Synnevag *et al.*, 2007), so this metric is included to quantify that change.

IV. RESULTS

A. Element Coupling

The effects of coupling on anechoic targets, wire targets, and in vivo rabbit tumor images can be observed in Figures 7, 8, and 9, respectively. As predicted by the beam patterns, higher degrees of coupling resulted in a loss to resolution. For DAS beamforming, FWHM estimates for the wire target at the bottom right increased from 0.78 mm to 2.09 mm between coupling factors 1 and 4. With alternative beamformers, resolution was adjusted back to 0.82 mm with MV for coupling by 4. The SCF beamformer had lower FWHM estimates, but that was only due to distortion in the lateral profile of the wire, which can be viewed in Figure 10. For coupling of 2, all beamformers exceeded the resolution of uncoupled DAS. Charts of all quality metrics for all beamformers are displayed in Figure 11.

In terms of contrast, element coupling also reduced the contrast ratio from -24 dB without coupling to -18 dB coupling by 4, while gCNR moved from 0.98 without coupling to 0.90 coupling by 4. The MV beamformer did not improve either contrast metric for any coupling factor. Meanwhile, the NSI and SCF beamformers improved the contrast ratio, but lowered the gCNR. The best contrast ratio on coupled elements was achieved by the SCF beamformer for coupling by 2, with a value of -25 dB. Yet SCF also resulted in the lowest gCNR for coupling by 2, with a value of 0.69. In general, we observed that while

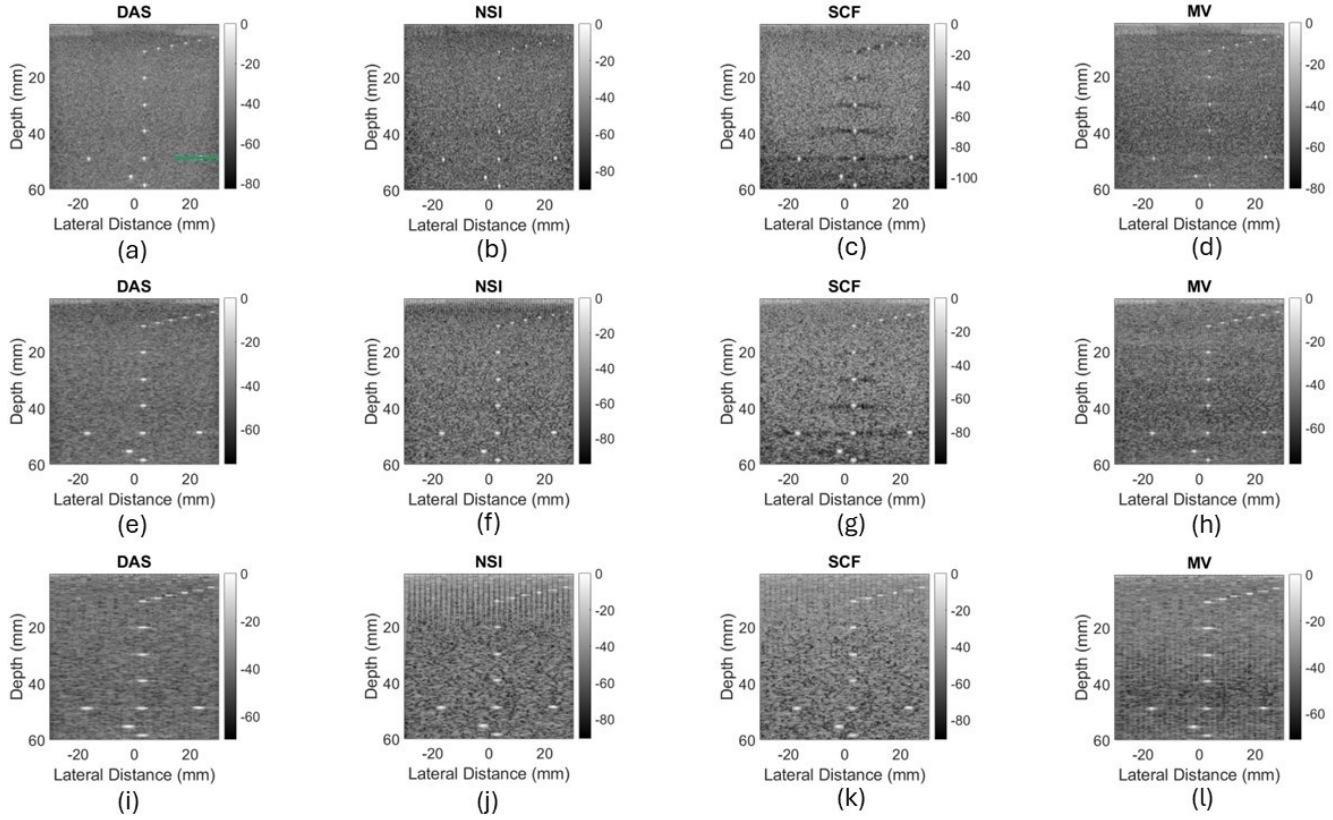


FIG. 7. Wire phantom images from different beamformers and coupling factors. **Top to bottom:** Coupling factors 1 (top), 2 (middle), and 4 (bottom). **Left to right:** DAS, NSI, SCF, MV. Note that each image is displayed with its full dynamic range.

alternative beamformers improved the contrast ratio for every coupling factor, they all also lowered the gCNR.

Element coupling slightly increased the sSNR values, going from 1.18 without coupling to 1.33 with coupling using DAS. The sSNR estimates were lower with the alternative beamformers, the lowest being 0.72 coming from NSI at a coupling factor of 4. Lastly, there was an increase in the size of a “dead zone” near the transducer face for higher coupling factors. This was manifest as the spike artifacts at the top of the images in Figures 7 and 8.

B. Increased aperture size

The resulting B-mode images of the virtual large aperture are displayed in Figure 12. Each of these images has a 120 mm FOV, double that of the L14-5/60, but the same number of elements as the 14-5/60. Many of the same quality observations can be made here as were made in the previous section. The main new observation for these images is the darker cone in the center of each image. This is an artifact of the acquisition setup, where data from either half of the virtual large aperture was collected separately. There was no way for the left half to transmit while the right half received or vice-versa, but pixels in the center rely on data from both halves

during beamforming. That data was missing due to the limitations in our setup, creating this artifact.

V. DISCUSSION

In our approach to increasing FOV, the most important consideration is the size of the elements and the effects that element size has on image quality. As predicted by the theoretical beam patterns, resolution decreased greatly for larger elements (i.e. higher coupling factors) due to the widened directivity and increased F-number. As a side effect of decreased resolution, the sSNR increased for higher coupling factors because of a larger resolution cell containing a higher number of scatterers. We observed that adaptive and non-linear beamformers could be used, not just to regain resolution, but actually exceed the resolution of uncoupled DAS images. The MV beamformer resulted in the highest resolution among the three alternative beamformers. Furthermore, this increase in resolution did not come with as great a cost to sSNR with MV as it did with NSI or SCF. Overall, the MV beamformer seemed the best fit for improving resolution for a large aperture based on the resolution and sSNR values. However, the major trade-off with MV is its computational complexity in inverting the spatial covariance matrix compared to NSI or SCF. This might not

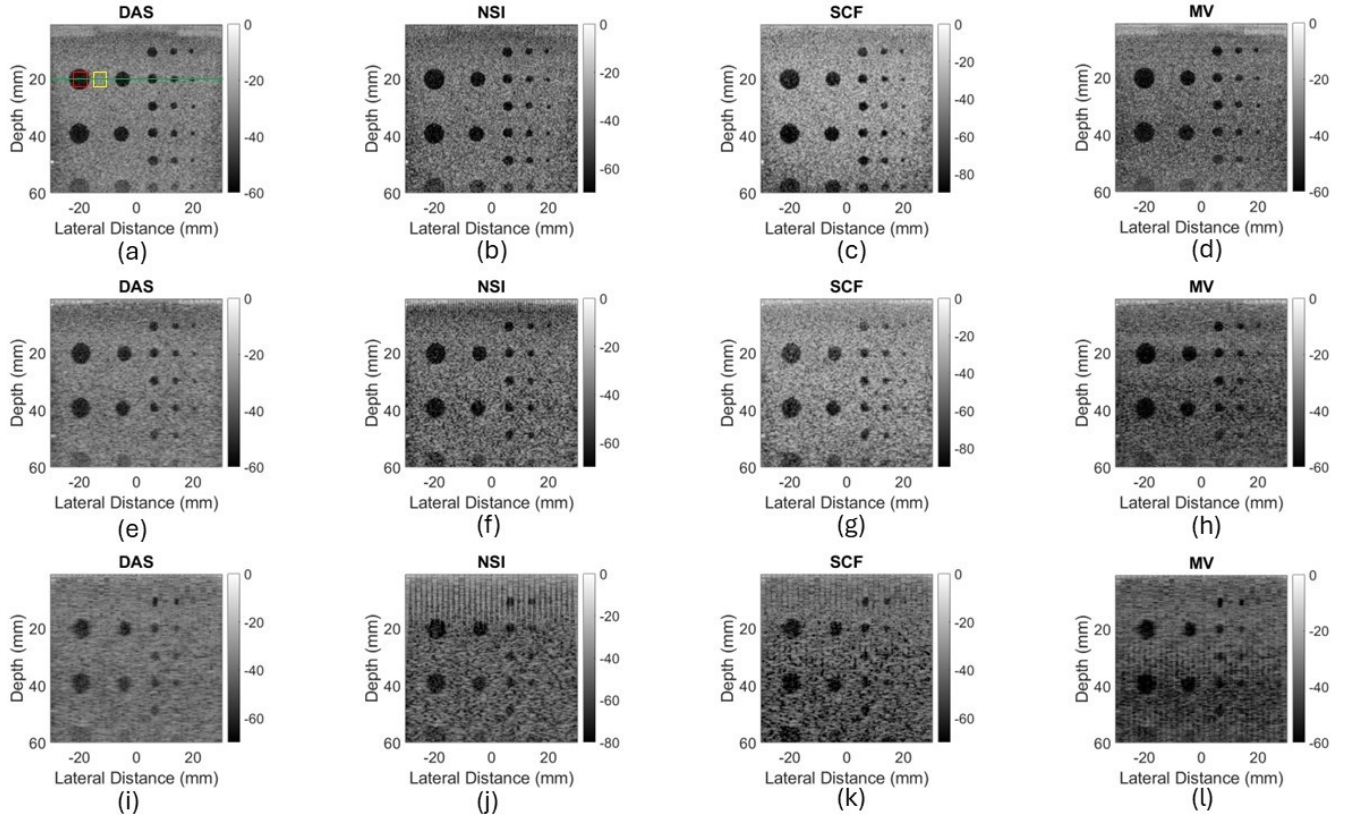


FIG. 8. Cyst phantom images from different beamformers and coupling factors. **Top to bottom:** Coupling factors 1 (top), 2 (middle), and 4 (bottom). **Left to right:** DAS, NSI, SCF, MV. Note that the dynamic range on each image was adjusted to make the speckle about the same brightness for all images.

be a major issue for B-mode imaging on large apertures, but would certainly be something to consider for large apertures if used for Doppler or shear wave. In those cases, NSI might be preferable for faster beamforming and high resolution (Kou *et al.*, 2023).

The coupled elements also resulted in slightly decreased contrast for both CR and gCNR metrics. This is likely a result of a decreased number of angles used for compounding with higher coupling factors (see Table I). Unfortunately, the alternative beamformers did not offer much improvement in this area. While the SCF beamformer improved contrast ratio the most, every beamformer lowered the gCNR values, suggesting that improvements to visual contrast (i.e. contrast ratio) are merely dynamic range changes imposed by the beamformers. Furthermore, there was an increase in “dead zone” size resulting from extremely narrow directivities of highly coupled elements. This is a region where only 1 or 2 elements contribute to each pixel according to the F-number, so none of the beamformers are effective. This would limit the use of large-element arrays for superficial applications, but they can still be clinically relevant for applications needing greater imaging depths, such as abdominal. For our experiments, we found that a coupling factor of 2, corresponding to an element size of 5

wavelengths, still produced high-resolution images over the whole region, including near the transducer face. Using this coupling factor, we were able to produce B-mode images with high resolution from a virtual large aperture of 120 mm width and 128 elements, demonstrating how larger apertures could be built using larger elements without increase to element count. Our goal is to take this approach to 2D matrix arrays, creating larger apertures using large square elements, and the results demonstrate for a 1D case the effectiveness of the approach.

The transmission sequence is an important consideration in a study on increased aperture size. In this study, we used plane-wave compounding for B-mode image reconstruction, using an optimal angle set derived from the equations in (Montaldo *et al.*, 2009). Based on these equations, different coupling factors and aperture sizes lead to different maximum angles, angular step sizes, and number of transmissions according to what spatial frequencies are available with a given array pitch. We chose to use the maximum number of angles available for a given coupling factor and aperture length in order to maximize both contrast and resolution. Unfortunately, the high number of angles will also limit potential frame rates. If higher frame rates are needed, the optimal angle set could be decimated at the cost of introducing grating

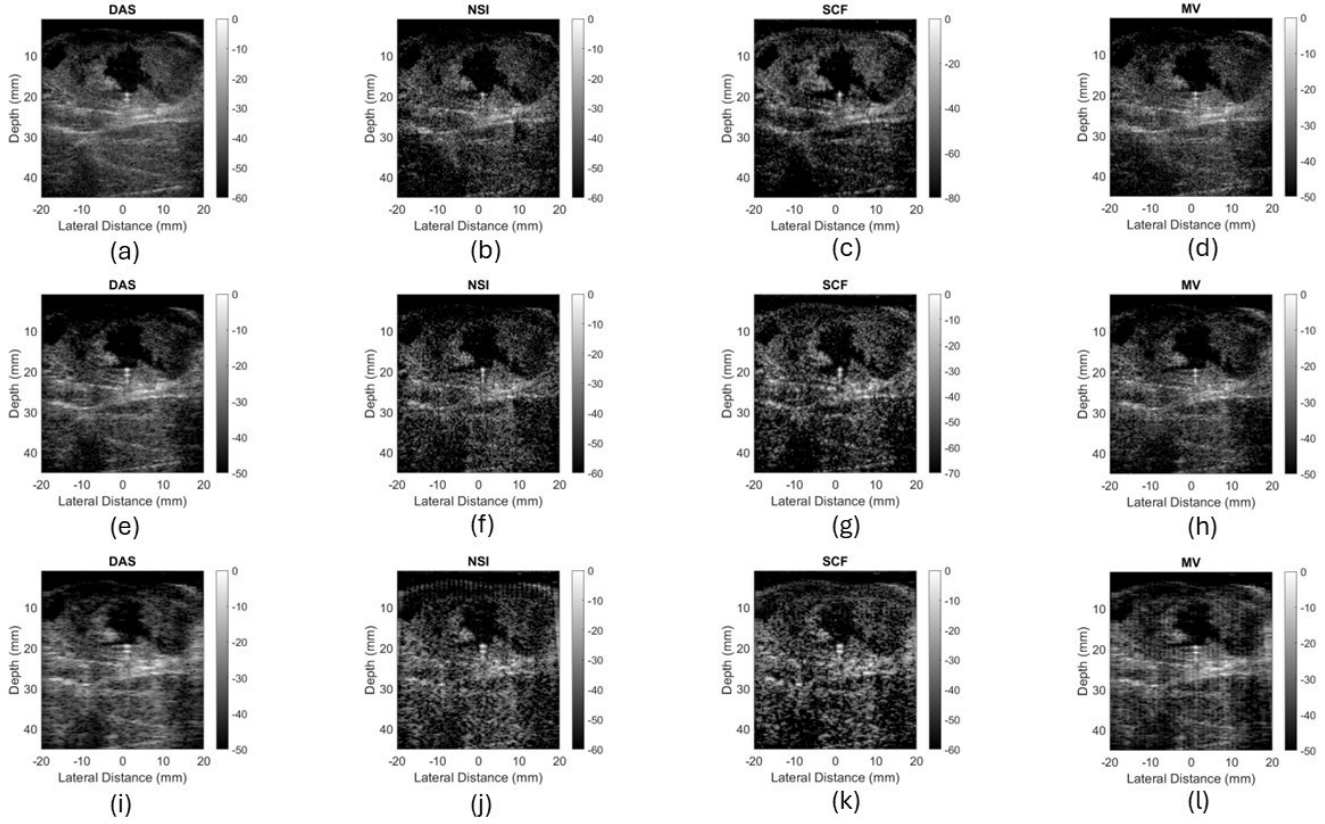


FIG. 9. In vivo rabbit tumor images from different beamformers and coupling factors. **Top to bottom:** Coupling factors 1 (top), 2 (middle), and 4 (bottom). **Left to right:** DAS, NSI, SCF, MV. Note that the dynamic range on each image was adjusted to make the speckle about the same brightness for all images.

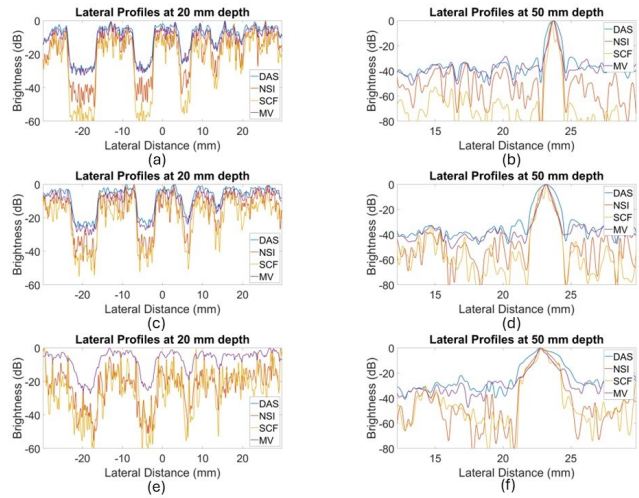


FIG. 10. Lateral profiles of anechoic regions (left column) and wire targets (right column) from the phantom experiments. **Top to bottom:** no coupling, coupling by 2, coupling by 4.

lobes into the synthesized transmit beam during compounding (Bae and Song, 2018; Denarie *et al.*, 2013). A more thorough study examining the effectiveness of

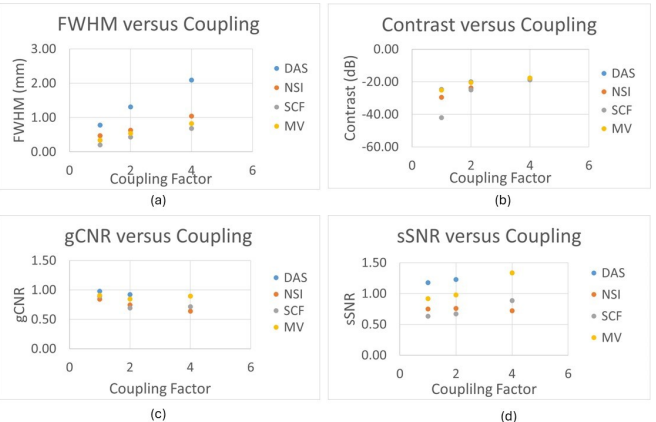


FIG. 11. Image quality metrics from the phantom experiments. The FWHM was estimated from the wire targets in Figure 7. The Contrast, gCNR, and sSNR were estimated from anechoic regions in Figure 8.

large-element arrays with other types of transmissions sequences, such as synthetic aperture, diverging wave, or focused beam, would be necessary to strengthen the clin-

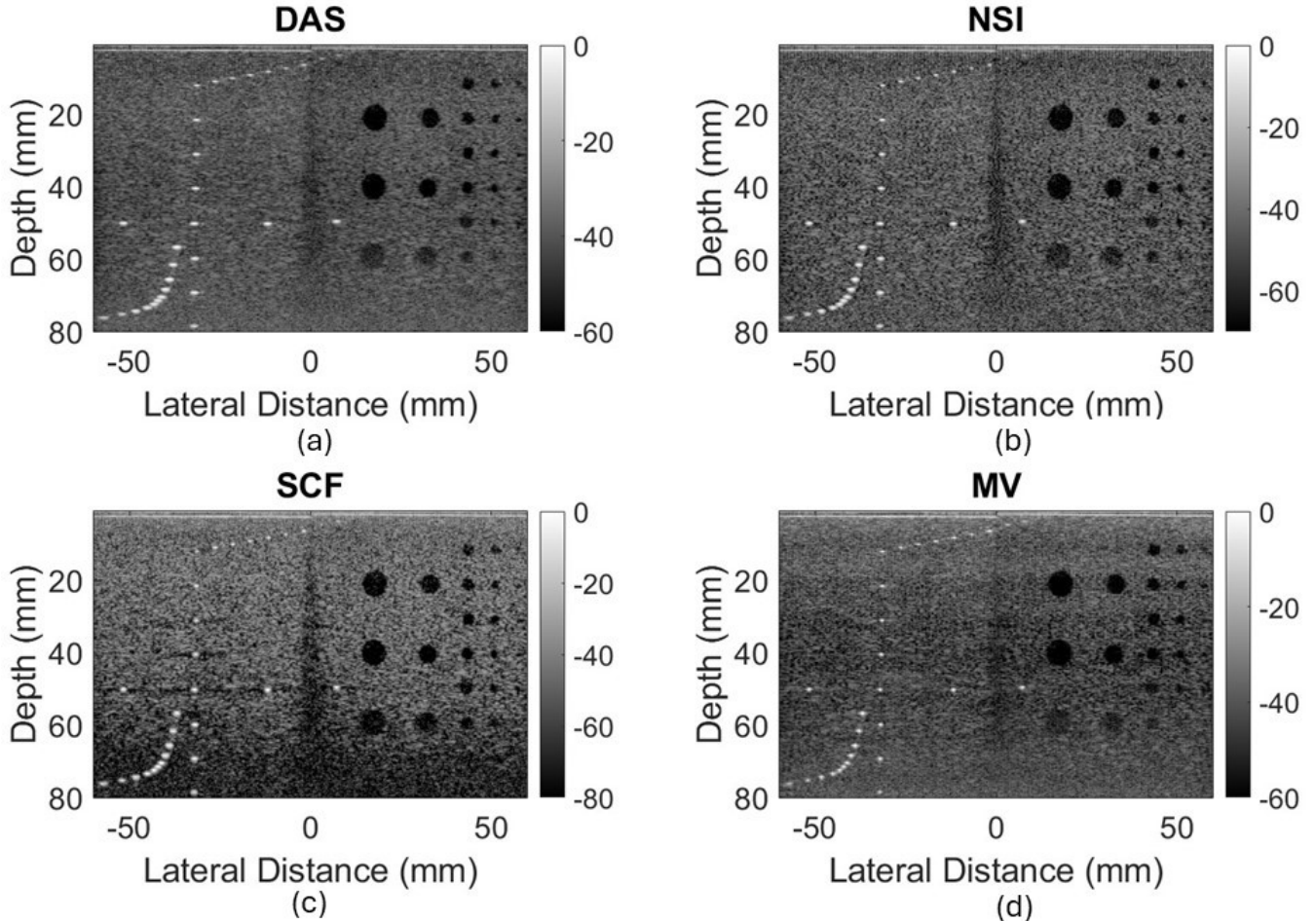


FIG. 12. B-mode images of a virtual large aperture made up of 128 elements with an element size of 5 wavelengths. Images were beamformed with (a) DAS, (b) NSI, (c) SCF, and (d) MV.

ical relevance of such large apertures, but is beyond the scope of this paper.

As a final consideration, with these beamformers, it is important to point out that parameter tuning affects the quality of their results significantly. Our particular values of tuning parameters were 1) a DC offset of $dc = 0.5$ for NSI (Eq. 14), 2) an exponent $p = 1$ for SCF (Eq. 19), and 3) sub-array size $M = N/2$ (N is number of receive elements) and diagonal loading factor $\Delta = \frac{1}{10M}$ for MV (Eqs. 21 and 23). The parameters for MV were chosen based on recommended values in the paper which introduced it for ultrasound B-mode imaging (Synnevag *et al.*, 2007). The parameters for NSI and SCF were chosen empirically to balance speckle suppression with resolution increase. While our results are limited to our chosen set of tuning parameters, the trade-offs of different tunings are known and already published in the literature (Agarwal *et al.*, 2019; Camacho *et al.*, 2009b; Synnevag *et al.*, 2007). In particular, in tuning for a resolution increase, all three beamformers will also result in

higher speckle variance, which can lead to underdeveloped speckle and reduce image contrast.

VI. CONCLUSION

This study was aimed at increasing ultrasound FOV using larger elements and adaptive or non-linear beamforming. We have demonstrated through Fourier transforms of elements how a minimum kerf is optimal to minimize grating lobes for an increased pitch. We also showed that coupled elements make a good approximation of large elements. Experiments were performed with coupled elements in phantoms and *in vivo* that demonstrated the resolution loss from an increased F-number with larger elements. However, our experiments also demonstrated how adaptive and non-linear beamformers, such as NSI, SCF, and MV could be used to not only regain resolution, but actually exceed the resolution of DAS beamforming on an uncoupled array. Using these alternative beamformers, high-resolution images were recon-

structed with elements up to 5 wavelengths wide. Even elements up to 10 wavelengths wide could be used with the trade-off of losing superficial regions of the image near the transducer face. With proper coupling and beam-forming, we have also directly shown how larger elements can lead to larger apertures by collecting data from a virtual large aperture using a positioning system. This virtual aperture had a width of 120 mm with only 128 elements. We see potential application of our approach for increasing the FOV of 2D ultrasound probes using larger square elements, which can greatly benefit applications such as abdominal or vascular imaging.

ACKNOWLEDGMENTS

This work was supported by the National Institutes of Health (NIH), grant numbers R01CA251939, R01CA273700, and R21EB024133.

AUTHOR DECLARATIONS

The authors have no competing interests to declare.

Animal procedures were approved by the Institutional Animal Care and Use Committee at the University of Illinois at Urbana-Champaign, protocol number 23062.

DATA AVAILABILITY

Data will be made available upon request.

Agarwal, A., Reeg, J., Podkowa, A. S., and Oelze, M. L. (2019). “Improving Spatial Resolution Using Incoherent Subtraction of Receive Beams Having Different Apodizations,” *IEEE Transactions on Ultrasonics, Ferroelectrics, and Frequency Control* **66**(1), 5–17, doi: [10.1109/TUFFC.2018.2876285](https://doi.org/10.1109/TUFFC.2018.2876285).

Bae, S., and Song, T.-K. (2018). “Methods for Grating Lobe Suppression in Ultrasound Plane Wave Imaging,” *Applied Sciences* **8**(10), 1881, doi: [10.3390/app8101881](https://doi.org/10.3390/app8101881).

Bottenuis, N., Pinton, G. F., and Trahey, G. (2020). “The Impact of Acoustic Clutter on Large Array Abdominal Imaging,” *IEEE transactions on ultrasonics, ferroelectrics, and frequency control* **67**(4), 703–714, doi: [10.1109/TUFFC.2019.2952797](https://doi.org/10.1109/TUFFC.2019.2952797).

Camacho, J., Parrilla, M., and Fritsch, C. (2009a). “Grating-lobes reduction by application of Phase Coherence Factors,” in *2009 IEEE International Ultrasonics Symposium*, pp. 341–344, doi: [10.1109/ULTSYM.2009.5441770](https://doi.org/10.1109/ULTSYM.2009.5441770), iSSN: 1948-5727.

Camacho, J., Parrilla, M., and Fritsch, C. (2009b). “Phase Coherence Imaging,” *IEEE Transactions on Ultrasonics, Ferroelectrics, and Frequency Control* **56**(5), 958–974, doi: [10.1109/TUFFC.2009.1128](https://doi.org/10.1109/TUFFC.2009.1128).

Castrignano, L., Tortoli, P., Matrone, G., Crocco, M., Savoia, A. S., and Ramalli, A. (2025). “On the Impact of Microbeamformers in 3-D High Frame Rate Ultrasound Imaging: A Simulation Study,” *IEEE Transactions on Biomedical Engineering* **72**(6), 1941–1950, doi: [10.1109/TBME.2025.3529198](https://doi.org/10.1109/TBME.2025.3529198).

Chavignon, A., Heiles, B., Hingot, V., Orset, C., Vivien, D., and Couture, O. (2022). “3D Transcranial Ultrasound Localization Microscopy in the Rat Brain With a Multiplexed Matrix Probe,” *IEEE Transactions on Biomedical Engineering* **69**(7), 2132–2142, doi: [10.1109/TBME.2021.3137265](https://doi.org/10.1109/TBME.2021.3137265).

Denarie, B., Tangen, T. A., Ekroll, I. K., Rolim, N., Torp, H., Bjästad, T., and Lovstakken, L. (2013). “Coherent Plane Wave Compounding for Very High Frame Rate Ultrasonography of Rapidly Moving Targets,” *IEEE Transactions on Medical Imaging* **32**(7), 1265–1276, doi: [10.1109/TMI.2013.2255310](https://doi.org/10.1109/TMI.2013.2255310).

Favre, H., Pernot, M., Tanter, M., and Papadacci, C. (2022). “Boosting transducer matrix sensitivity for 3D large field ultrasound localization microscopy using a multi-lens diffracting layer: a simulation study,” *Physics in Medicine & Biology* **67**(8), 085009, doi: [10.1088/1361-6560/ac5f72](https://doi.org/10.1088/1361-6560/ac5f72).

Favre, H., Pernot, M., Tanter, M., and Papadacci, C. (2023). “Transcranial 3D ultrasound localization microscopy using a large element matrix array with a multi-lens diffracting layer: an *in vitro* study,” *Physics in Medicine & Biology* **68**(7), 075003, doi: [10.1088/1361-6560/acbde3](https://doi.org/10.1088/1361-6560/acbde3).

Foiret, J., Cai, X., Bendjador, H., Park, E.-Y., Kamaya, A., and Ferrara, K. W. (2022). “Improving plane wave ultrasound imaging through real-time beamformation across multiple arrays,” *Scientific Reports* **12**(1), 13386, doi: [10.1038/s41598-022-16961-2](https://doi.org/10.1038/s41598-022-16961-2).

Gardner, M., Miller, R. J., and Oelze, M. L. (2024). “Grating lobe mitigation on large-pitch arrays using null subtraction imaging,” *Ultrasonics* **140**, 107302, doi: [10.1016/j.ultras.2024.107302](https://doi.org/10.1016/j.ultras.2024.107302).

Gavrilov, L., Hand, J., Abel, P., and Cain, C. (1997). “A method of reducing grating lobes associated with an ultrasound linear phased array intended for transrectal thermotherapy,” *IEEE Transactions on Ultrasonics, Ferroelectrics, and Frequency Control* **44**(5), 1010–1017, doi: [10.1109/58.655626](https://doi.org/10.1109/58.655626).

Huang, Q., Deng, Q., Li, L., Yang, J., and Li, X. (2019). “Scoliotic Imaging With a Novel Double-Sweep 2.5-Dimensional Extended Field-of-View Ultrasound,” *IEEE Transactions on Ultrasonics, Ferroelectrics, and Frequency Control* **66**(8), 1304–1315, doi: [10.1109/TUFFC.2019.2920422](https://doi.org/10.1109/TUFFC.2019.2920422).

Jensen, J. A., Schou, M., Jørgensen, L. T., Tomov, B. G., Stuart, M. B., Traberg, M. S., Taghavi, I., Øygaard, S. H., Ommen, M. L., Steenberg, K., Thomsen, E. V., Panduro, N. S., Nielsen, M. B., and Sørensen, C. M. (2022). “Anatomic and Functional Imaging Using Row–Column Arrays,” *IEEE Transactions on Ultrasonics, Ferroelectrics, and Frequency Control* **69**(10), 2722–2738, doi: [10.1109/TUFFC.2022.3191391](https://doi.org/10.1109/TUFFC.2022.3191391).

Kang, J., Go, D., Song, I., and Yoo, Y. (2020). “Wide Field-of-View Ultrafast Curved Array Imaging Using Diverging Waves,” *IEEE Transactions on Biomedical Engineering* **67**(6), 1638–1649, doi: [10.1109/TBME.2019.2942164](https://doi.org/10.1109/TBME.2019.2942164).

Kim, S. H., Choi, B. I., Kim, K. W., Lee, K. H., and Han, J. K. (2003). “Extended Field-of-View Sonoigraphy,” *Journal of Ultrasound in Medicine* **22**(4), 385–394, doi: [10.7863/jum.2003.22.4.385](https://doi.org/10.7863/jum.2003.22.4.385).

Kou, Z., Lowerison, M., You, Q., Wang, Y., Song, P., and Oelze, M. L. (2023). “High-resolution Power Doppler Using Null Subtraction Imaging” doi: [10.48550/arXiv.2301.03719](https://doi.org/10.48550/arXiv.2301.03719).

Kou, Z., Miller, R. J., and Oelze, M. L. (2022). “Grating Lobe Reduction in Plane-Wave Imaging With Angular Compounding Using Subtraction of Coherent Signals,” *IEEE Transactions on Ultrasonics, Ferroelectrics, and Frequency Control* **69**(12), 3308–3316, doi: [10.1109/TUFFC.2022.3217993](https://doi.org/10.1109/TUFFC.2022.3217993).

Montaldo, G., Tanter, M., Bercoff, J., Benech, N., and Fink, M. (2009). “Coherent plane-wave compounding for very high frame rate ultrasonography and transient elastography,” *IEEE Transactions on Ultrasonics, Ferroelectrics, and Frequency Control* **56**(3), 489–506, doi: [10.1109/TUFFC.2009.1067](https://doi.org/10.1109/TUFFC.2009.1067).

Noorkoiv, M., Nosaka, K., and Blazevich, A. J. (2010). “Assessment of quadriceps muscle cross-sectional area by ultrasound extended-field-of-view imaging,” *European Journal of Applied Physiology* **109**(4), 631–639, doi: [10.1007/s00421-010-1402-1](https://doi.org/10.1007/s00421-010-1402-1).

Perrot, V., Polichetti, M., Varray, F., and Garcia, D. (2021). “So you think you can DAS? A viewpoint on delay-and-sum beamforming,” *Ultrasonics* **111**, 106309, doi: [10.1016/j.ultras.2020.106309](https://doi.org/10.1016/j.ultras.2020.106309).

Poon, T. C., and Rohling, R. N. (2006). “Three-dimensional extended field-of-view ultrasound,” *Ultrasound in Medicine & Biology* **32**(3), 357–369, doi: [10.1016/j.ultrasmedbio.2005.11.003](https://doi.org/10.1016/j.ultrasmedbio.2005.11.003).

Ramalli, A., Boni, E., Roux, E., Liebgott, H., and Tortoli, P. (2022). “Design, Implementation, and Medical Applications of 2-D Ultrasound Sparse Arrays,” *IEEE Transactions on Ultrasonics, Ferroelectrics, and Frequency Control* **69**(10), 2739–2755, doi: [10.1109/TUFFC.2022.3162419](https://doi.org/10.1109/TUFFC.2022.3162419).

Rodriguez-Molares, A., Rindal, O. M. H., D’hooge, J., Måsøy, S.-E., Austeng, A., Lediju Bell, M. A., and Torp, H. (2020).

"The Generalized Contrast-to-Noise Ratio: A Formal Definition for Lesion Detectability," *IEEE Transactions on Ultrasonics, Ferroelectrics, and Frequency Control* **67**(4), 745–759, doi: [10.1109/TUFFC.2019.2956855](https://doi.org/10.1109/TUFFC.2019.2956855).

Savord, B., and Solomon, R. (2003). "Fully sampled matrix transducer for real time 3D ultrasonic imaging," in *IEEE Symposium on Ultrasonics, 2003*, Vol. 1, pp. 945–953 Vol.1, <https://ieeexplore.ieee.org/document/1293556>, doi: [10.1109/ULTSYM.2003.1293556](https://doi.org/10.1109/ULTSYM.2003.1293556).

Synnevag, J. F., Austeng, A., and Holm, S. (2007). "Adaptive Beamforming Applied to Medical Ultrasound Imaging," *IEEE Transactions on Ultrasonics, Ferroelectrics, and Frequency Control* **54**(8), 1606–1613, doi: [10.1109/TUFFC.2007.431](https://doi.org/10.1109/TUFFC.2007.431).

Wagner, R., Smith, S., Sandrik, J., and Lopez, H. (1983). "Statistics of Speckle in Ultrasound B-Scans," *IEEE Transactions on Sonics and Ultrasonics* **30**(3), 156–163, doi: [10.1109/T-SU.1983.31404](https://doi.org/10.1109/T-SU.1983.31404).

Wang, Y., Zheng, C., Wang, Y., Liu, M., and Peng, H. (2022). "Wide Field-of-View Plane Wave Ultrasound Imaging based on Linear Array Sub-apertures and Adaptive Weighting Technique," in *2022 IEEE International Ultrasonics Symposium (IUS)*, pp. 1–4, doi: [10.1109/IUS54386.2022.9958863](https://doi.org/10.1109/IUS54386.2022.9958863).

Yu, J., Yoon, H., Khalifa, Y. M., and Emelianov, S. Y. (2020). "Design of a Volumetric Imaging Sequence Using a Vantage-256 Ultrasound Research Platform Multiplexed With a 1024-Element Fully Sampled Matrix Array," *IEEE Transactions on Ultrasonics, Ferroelectrics, and Frequency Control* **67**(2), 248–257, doi: [10.1109/TUFFC.2019.2942557](https://doi.org/10.1109/TUFFC.2019.2942557).